IEEE Access
Multidisciplinary | Rapid Review | Open Access Journal

Received 3 March 2023, accepted 15 March 2023, date of publication 24 March 2023, date of current version 25 July 2023.

Digital Object Identifier 10.1109/ACCESS.2023.3261565

RESEARCH ARTICLE

U-Grooved Selectively Coated and Highly Sensitive PCF-SPR Sensor for Broad Range Analyte RI Detection

ABDULLAH MOHAMMAD TANVIRUL HOQUE[1], KUSAY FAISAL AL-TABATABAIE[2], MD. EAKUB ALI[1], ASAD MUHAMMAD BUTT[3], SHEIKH SHARIF IQBAL MITU[4], (Senior Member, IEEE), AND KHURRAM KARIM QURESHI[4], (Senior Member, IEEE)

[1]Department of Electrical and Electronic Engineering, Bangabandhu Sheikh Mujibur Rahman Science and Technology University, Gopalganj 8100, Bangladesh
[2]Department of Computer Science, Cihan University, Sulaimaniya Campus, Sulaimaniya, Kurdistan 46001, Iraq
[3]College of Chemicals and Materials, King Fahd University of Petroleum and Minerals, Dhahran 3126, Saudi Arabia
[4]Department of Electrical Engineering and Center for Communication Systems and Sensing, King Fahd University of Petroleum and Minerals, Dhahran 3126, Saudi Arabia

Corresponding authors: Asad Muhammad Butt (asad.arshad@kfupm.edu.sa) and Khurram Karim Qureshi (kqureshi@kfupm.edu.sa)

This publication is based on the work supported by King Fahd University of Petroleum and Minerals (KFUPM), Dhahran, Saudi Arabia. The authors acknowledge the Deanship of Research Oversight and Coordination. Khurram Karim Qureshi would also like to acknowledge the support provided by Interdisciplinary Research Center for Communication Systems and Sensing through project no. INCS2303.

ABSTRACT Point-of-care (POC) diagnostic medical devices require simple but sensitive and inclusive detection capabilities. This study develops a unique photonic crystal fiber-based surface plasmon resonance (PCF-SPR) sensor that uses a u-grooved selective coating for extremely sensitive remote and biosensing applications. Scale-down (SCD) air holes control the path that incoming light takes through the sensor in order to activate the free electrons that are present there. To reduce outward radiation, perfectly matched layers (PML) of the absorbing boundary are integrated in addition to optimizing the structural geometry and material thickness. The Finite Element Method (FEM) is employed to quantitatively tune the properties of light and sensitivity of the proposed sensor. The proposed sensor has the maximum amplitude sensitivity (AS) of 1189 RIU^{-1}, the highest wavelength sensitivity (WS) of 12,500 nm/RIU, and an outstanding resolution of 8.0×10^{-6} RIU. The constructed model covers a large refractive index (RI) range of unknown samples, ranging from 1.29 to 1.40. This range allows the proposed sensor to cover the detection of a wide range of bio-analytics, including viruses, cancer cells, carbohydrates, proteins, and DNA/RNA, etc. We strongly believe that the proposed sensor will play an extremely useful role in the detection of POC bio-sample detection.

INDEX TERMS PCF, sensitivity, resolution, SPR, refractive index, COMSOL multiphysics, FEM.

I. INTRODUCTION

Surface plasmon resonance (SPR) is a well-known and well-established method for detecting refractive index (RI) [1], [2]. In contrast to prism-based SPR sensors, which have bulky systems, configurational structures with limited wavelengths, and waveguides with V-grooves, the PCF-SPR-based sensors have gained popularity due to several significant advantages, such as high precision, accessibility, real-time, and label-free sensing properties [3]. Additionally, optical fiber is given priority over the conventional type SPR sensors, as an excellent option for cheap and miniaturized sensors to drive the surface plasmon polaritons (SPP) modes [3]. Noticeably, the freedom offered by photonic crystal fiber (PCF) to synthesize the optical variables, arrangeable geometry of formation, and manageable birefringence, makes it useful for a broad range of sensing capabilities [4]. Hitherto, a lot of research has been reported using PCF-based SPR sensing technology, since they can be extensively implemented in diverse sensing fields, such as living organisms, and chemical and

The associate editor coordinating the review of this manuscript and approving it for publication was Santosh Kumar.

biological substances [5], [6], [7], [8], [9]. Wide detection range, adjustable dispersion, high-level integration, excellent propagation, miniature size, and extremely sensitive properties are some of the fundamental benefits of using PCF-SPR-based sensors [10], [11], [12]. Mostly Au, Ag, Cu, Al, Pd, and Bi play a significant role as the plasmonic materials in the PCF-SPR based sensing techniques. Au exhibits stability in chemical processes due to its resonant peak variation than other plasmonic materials [13], [14]. Typically single analyte-type PCF-SPR sensors have been reported [10], [13], [15]. Ayyanar et al. recently revealed an external type D-shaped PCF sensor, utilizing Au/Ge2Sb2Te5 as a sensing layer for the detection of individual analyte, where optimum WS for crystalline and amorphous phases are 17,600 nm/RIU and 8,000 nm/RIU respectively [6]. Dash et al. also disclosed a single analyte type sensor that achieved highest WS of 2,000 nm/RIU and optimized for the analyte RI range from 1.33 to 1.35 [16]. Jahan et al. introduced an external sensing technique using a PCF sensor that achieved a maximum WS and AS of 20,000 nm/RIU and 1380 RIU^{-1} respectively [17]. Poli et. al reported a multi-analyte PCF sensor with internal coating having a peak WS of 18,000 nm/RIU [5]. Kaur and Singh has also introduced a multianalyte SPR model with optimum WS of 3,750 nm/RIU [18]. Jabin et. al has proposed a titanium coated external type individual sample biosensor with WS of 10000 nm/RIU for x-polarization [19]. Biplob Hossain et al. proposed a PCF sensor that was optimized for RI in the range 1.42-1.46 and exhibited the maximum WS and AS of 15000 nm/RIU and 230 RIU^{-1} respectively [20]. Kaur and Singh proposed PCF-SPR-based sensor design, which was optimized for the refractive index in the range of 1.385-1.40, and produced a maximum wavelength sensitivity of 10,000 nm/RIU [21]. Anik et al. proposed a structure that was optimized for RI covering 1.14-1.36 and with optimum AS and Figure of Merit (FOM) values of 328 RIU^{-1} and 105 RIU^{-1} respectively [22]. A circular shaped PCF sensor was designed by Dash et al. which exhibited the highest WS and resolution of 2000 nm/RIU and 5×10^{-5} RIU respectively [23]. With the main objective of detailing the broad variety of its applications for biomedical sensors, including DNA, protein, and glucose sensing. Rachana et al. carried out a study for different PCF shapes in biomedical sensors [24]. All the proposed sensors mentioned above are implemented by either using internal or external techniques. In case of the internal sensing technique, the internal surface coating of selective holes with plasmonic materials that is usually 1-2 μm thick infiltrate the liquid that make this technique slightly complex during the fabrication. On the other hand, in case of the external type sensing technique, the complexity in the internal type sensing approach could be overcome even though sometimes this technique may depict less sensitivity due to long distance interaction between core and plasmonic layers [25], [26]. Nevertheless, the primary purpose for modeling this PCF based SPR sensor is to improve the maximum coupling outcome between plasmonic and the elemental modes by optimizing the forming factors; such as air holes pitch, diameter, ring lattice setting, as well as the selection of plasmonic materials.

In this work, an internal type ring-shaped single analyte biosensing technique is proposed to detect broad range RI of bio-samples. For internal sensing approach, this PCF-SPR sensing technique can be a solution due to its outstanding features and outcomes. Due to its novelty compared to previously published sensors and the proximity of its core to the internal sensing channel, which enhances performance, the sensor may lower the cost of plasmonic materials and low sensitivity limitations. Passing the propagating light through the scale down (SCD) air-holes excite the channel of the PCF, causing improved RI sensing. Therefore, the sensor can be used with high accuracy to detect a broad range of unknown analyte's RI from 1.29 to 1.40. We have chosen Au as the plasmonic material for this model due to its advantages over others. The highest sensitivity achieved for the wavelength and amplitude interrogation techniques are 12,500 nm/RIU and 1189 RIU^{-1} respectively. Finally, the proposed sensor has shown promising results, such as outstanding sensitivity and spectral interrogation. The configurational parameters, like plasmonic material, pitch size, SCD air holes diameter, analyte and gold layer thicknesses are fabricated in such a way to achieve the proper detection of the analyte.

II. THEORY AND SENSOR MODELING

Fig. 1(a), shows the cross-sectional view of the proposed model, where the smallest air hole is located in the center to facilitate the phase matching of elementary core mode with SPP modes, while for instigating the birefringence effect, five smaller SCD air holes are introduced that surrounds the center air hole. In addition, another motive for introducing these SCD air holes is to fix the sufficient leakage of energy of the evanescent field to the plasmonic layer that excites the surface plasmons with appropriate efficacy.

The stacked preform of the proposed model is shown in Fig. 1(b), where the hexagonal composition of the proposed sensor is designed with three different circular types of SCD air holes. They aid in creating the evanescent field, necessary to excite the electrons already present on the metal surface. In terms of fabrication, the distance between the two SCD air holes, called the pitch size has a value of 2.2 μm. The regular SCD air holes are shown by thick wall capillary and has the diameter of $d = 1.76$ μm. The small SCD air holes are represented by thin wall capillary and has the diameter of $d_s = 0.5$ μm. Finally, the smallest SCD air holes are shown by thinner wall capillary with a diameter of $d_c = 0.264$ μm. The solid rod indicates that there is no air hole at that position. In addition, the gold layer thickness of $t_g = 45$ nm, liquid layer thickness of $t_{AL} = 1$ μm and PML layer thickness of $t_{PML} = 2.0$ μm have been chosen for the proposed structure. By using the Sellmeier equation, we can evaluate the refractive index of the fused silica [27].

$$n^2 = 1 + \frac{B_1\lambda^2}{\lambda^2 - C_1} + \frac{B_2\lambda^2}{\lambda^2 - C_2} + \frac{B_3\lambda^2}{\lambda^2 - C_3} \quad (1)$$

where λ is the wavelength in μm, n is the RI of the fused silica, $B_i = 1,2,3$ and $C_i = 1,2,3$ are Sellmeier constants and the approximate magnitudes of these constants are available in [28]. The availability of sufficient free electrons on the metal surface determine the affinity of analyte ligand binding when the energy transaction occurs. The electrical property of the plasmonic material directly modulates the sensitivity of the sensor.

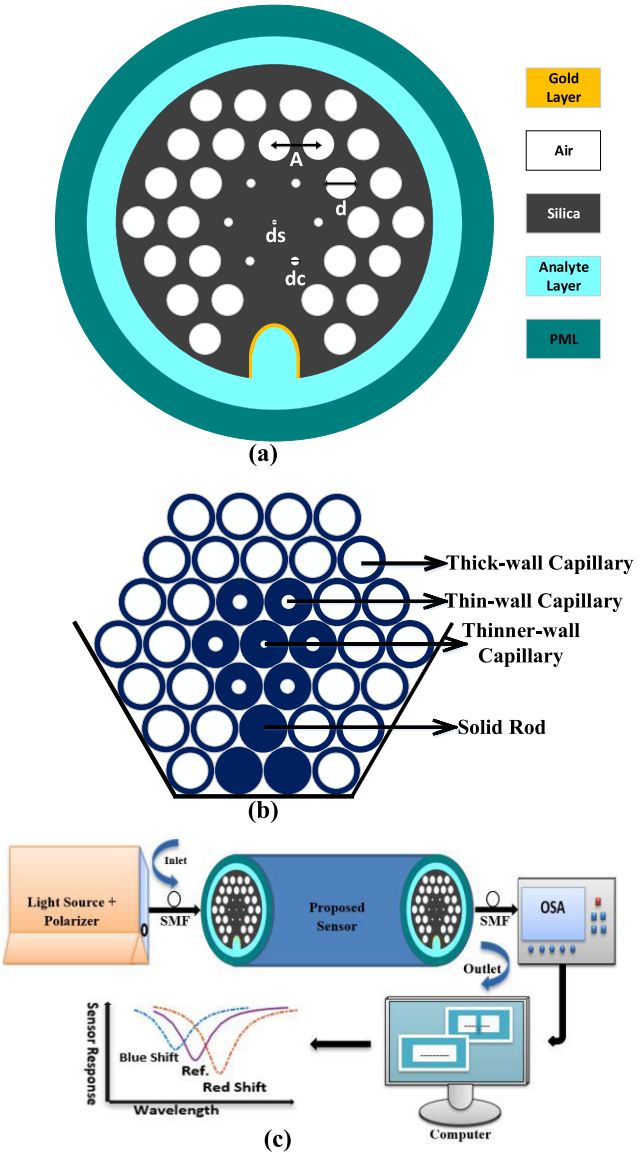

FIGURE 1. (a) Cross-sectional view of the suggested sensor, where d = 1.76 μm, d_s = 0.5 μm, d_c = 0.264 μm, t_g = 45 nm, t_{AL} = 1 μm, and t_{PML} = 2.0 μm (b) Suggested PCF's preform structure and (c) Proposed experimental setup.

The Drude-Lorenz model can be used to calculate the dielectric constant of Au [28].

$$\varepsilon_{Au} = \varepsilon_{\infty} - \frac{\omega_D^2}{\omega\left(\omega + j\lambda_D\right)} - \frac{\Delta\omega\Omega_L^2}{\left(\omega^2 - \Omega_L^2\right) + j\Gamma_L\omega} \qquad (2)$$

where the permittivity of Au is denoted by ε_{Au} at a high frequency, ε_{∞} represents the permittivity at a constant value of 5.9673, and the angular frequency can be expressed as $\omega = 2\pi c/\lambda$ where c indicates the velocity of light in free space. The plasmon frequency and damping wavelength are denoted by ω_D and λ_D whereas the magnitude of $\omega_D/2\pi$ and $\lambda_D/2\pi$ are 2113.6 THz and 15.92 THz respectively. $\Delta\varepsilon$ denotes the weighting factor, while $\Gamma_D/2\pi$ represents the spectral width and $\Omega_L/2\pi$ stands for the oscillator strength, which have the magnitudes of 104.86 THz and 650.07 THz respectively [28].

Fig. 1(c) depicts the experimental set-up, where a broadband or monochromatic light source can be utilized. As shown in the figure, a transverse magnetic or p-polarized electromagnetic wave is initially transmitted through the single-mode PCF by a light source. As a result, the electromagnetic wave gradually loses its intensity due to the dissipation of plasmonic energy at the interface. The maximum power is received by the SPP at the resonant wavelength, which is dependent on the RI of specific liquid streaming over the surface of the sensor. A computer-connected photodetector or optical spectrum analyzer (OSA) is employed in order to interpolate and fine-tune the loss curves and compare the sensor's response with the pre-trained reference spectrum by the computer's processing unit. Finally, a user-defined decision tree algorithm indicates the RI of the unknown sample on a display unit.

In Fig. 2, the propagation loss and AS curves are depicted for different types of plasmonic materials. Fig. 2(a) is illustrated for Indium-Tin-Oxide (ITO) metal that shows the peak confinement losses of 39 dB/cm and 51 dB/cm for RI of 1.35 and 1.36 respectively, and the WS and AS for ITO are respectively 100 nm/RIU and 63 RIU^{-1}. Fig. 2(b) depicts the peak confinement losses for Au of 30 dB/cm and 34 dB/cm for RI of 1.35 and 1.36 respectively. The WS and AS are 2000 nm/RIU and 159 RIU^{-1} respectively, which are higher than ITO. The comparative data for the different plasmonic materials is shown in Table 1. It is quite evident that gold is quite appropriate as a plasmonic material in our proposed sensor, since it has comparatively better response.

A. SPP EXCITATION

The working principle for the SPR sensor depends on the interaction between the evanescent field and the metal overlay, where the propagating light beam penetrating in the cladding area results in evanescent field. The real portion of the effective RI of the core and the surface plasmon have equal value at the resonant point, while surface plasmon ripple is generated due to the excitation of the free electrons by the core-cladding evanescent field in the metal surface. Thus, a clearly marked optimum loss is found at the resonant point and the unknown analyte RI can be identified by the variation of wavelength and amplitude. Furthermore, there are two fundamental modes due to the effect of birefringence.

Fig.3 depicts the electric field distribution characteristics of the developed sensor's y-polarized mode as well as the

cohesion between the core and SPP modes. In Fig. 3(a) and Fig. 3(b), the core and SPP modes are shown for the analyte RI of 1.35, where the fractional fluctuation in the analyte RI affects the real refractive index parameters of the core and SPP modes. It is apparent that these two polarized modes have huge difference. Fig. 3(c) illustrates the phase matching phenomenon at a sample RI of 1.35, which is the dispersion connection between the core and SPP modes. The definitions of real (n_{eff}) for core guided and SPP modes for y-polarized mode are given in the legends of Fig. 3(c). The core-guided mode and SPP mode's real (n_{eff}) are indicated by the solid and dotted orange lines respectively.

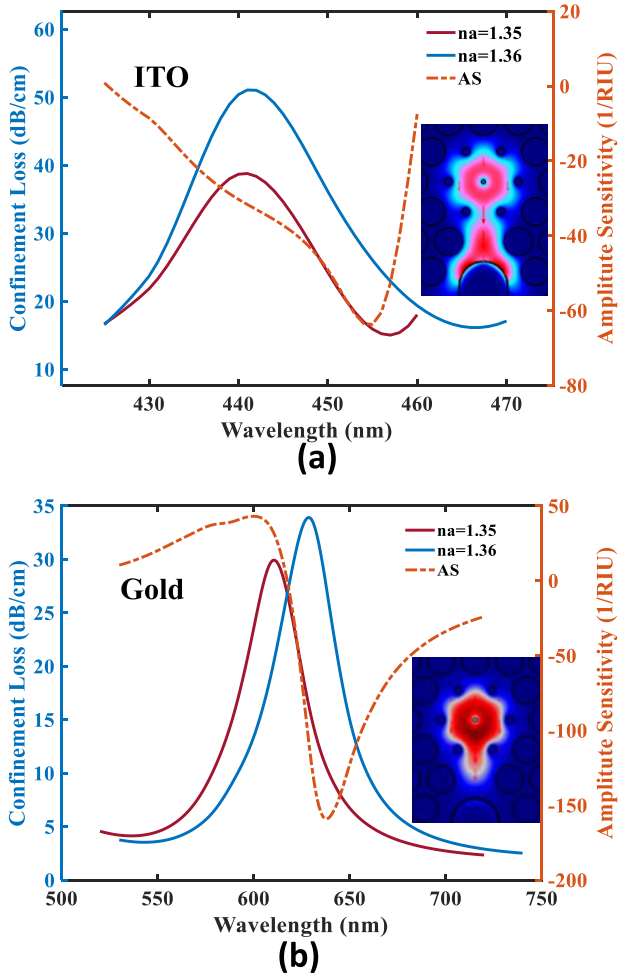

FIGURE 2. Confinement loss and AS curve (a) when ITO is a plasmonic material and, (b) when Gold is a plasmonic material.

In addition, the coupled point for the index of core and SPP modes is found at 610 nm, and at this intersection point, maximum power is transferred from core to SPP modes [29]. The phase matching technique can be justified by the coincidence of the coupled point and the peak loss that occurred at the resonant wavelength. However, we achieved an explicit model since the phase-matching requirement is almost precise at the resonant wavelength for RI of 1.35 for the y-polarized mode.

TABLE 1. Precision data for plasmonic material selection.

Plasmonic Material	Resonant Wavelength (nm)	Propagation Loss (dB/cm)	WS (nm/RIU)	AS (RIU^{-1})
ITO	441 (1.35) 442 (1.36)	39 51	100	63
Au	610 (1.35) 630 (1.36)	30 34	2000	159

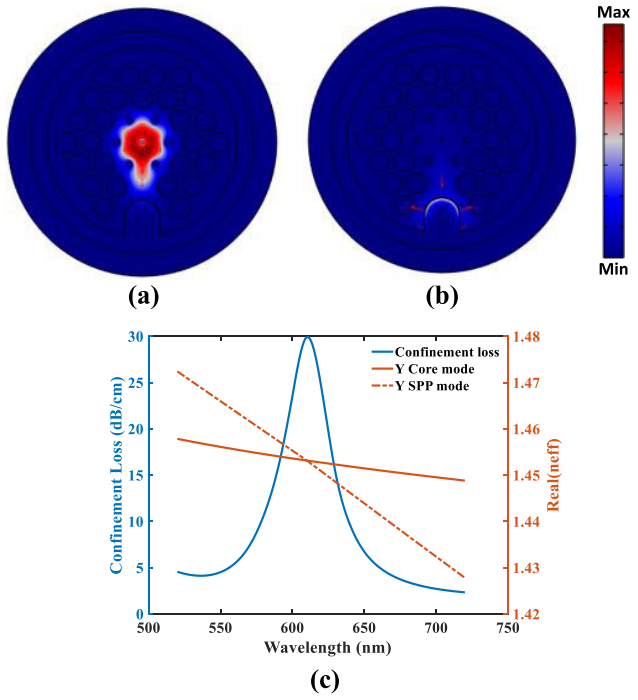

FIGURE 3. (a) Distribution of y -polarized electric fields of core-guided mode (b) SPP mode and (c) y-polarized phase-matching condition at analyte RI of 1.35.

B. MODEL ANALYSIS

In order to evaluate the SPR properties, the confinement loss can be measured by the following equation [30].

$$\alpha(dB/cm) = 8.686 \times k_0 \times I_m(neff) \times 10^4 \qquad (3)$$

where $k_0 = 2\pi/\lambda$ indicates propagation constant in free space. The functional portion of the RI is symbolized by $I_m(n_{eff})$ and λ indicates the operational wavelength. Due to slight discrepancy in RI value, the real portion of n_{eff} of the SPP mode varies, which results in varying the wavelength of phase matching. In addition, the phase matching wavelength variations display either red or blue shifting characteristics due to RI variations of the analyte [10]. In Fig. 4(a), the loss curves due to the variation of the analyte RI from 1.29 to 1.40 are presented. It shows the red shifting characteristics, since the resonant phase matching points are being shifted towards the higher wavelength with respect to the increment of the sample's RI. Thus, the shortest and longest resonant

wavelengths are found for the sample RI of 1.29 and 1.40 respectively.

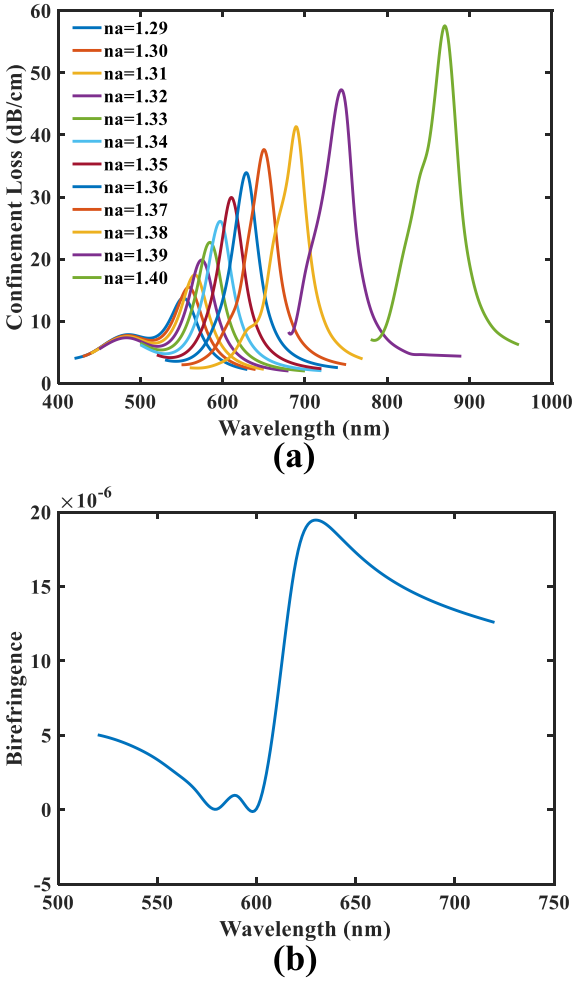

FIGURE 4. (a) Wavelength shift of propagation loss peaks with different RIs of liquid (b) Birefringence characteristics of the proposed sensor.

Fig. 4(a) also reveals the reduced energy shifting from core mode to its SPP mode [31]. The resonant wavelength for the analyte RI of 1.29 appears at 553 nm for y-polarized mode and the corresponding loss spectrum is 13.6 dB/cm. The red shifting property and the index differences of core and SPP modes results in variation of the confinement loss [28]. On the other hand, the resonant wavelength for the analyte RI of 1.40 appears at 870 nm and the corresponding loss spectrum is 57.6 dB/cm. However, the proposed model constitutes the highest WS of 12,500 nm/RIU. Usually, with the increase of sample refractive index, the contrast of RI of core and SPP modes causes the strong coupling, as a consequence, the sensor can be made more sensitive. Therefore, the sensor will exhibit an increased sensitivity with the analyte RI, which may lead to a nonlinear sensing response [32]. Fig. 4(b) shows the suggested sensor's birefringence characteristics, which is illustrated for the sample RI of 1.38. The following equation can be used to calculate the sensor's birefringence feature [33]:

$$B = \left| n_x - n_y \right| \tag{4}$$

where the refractive index of x and y polarized modes are denoted by n_x and n_y respectively [34]. According to Fig. 4(b), a significant variation between the two polarized modes is caused by birefringence, which grows gradually with the forward shifting of the operational wavelength. The large discrepancies suggest that the proposed model represents massive light coupling and forward movement of the peak wavelength in the x or y polarized modes, that generates more SPP on the dielectric interface of the metal [35].

III. COMPUTATION OF SENSOR PERFORMANCE

A. SENSITIVITY

Using AS and WS techniques, the sensitivity of the sensor is calculated. When compared with the amplitude interrogation technique, the wavelength interrogation technique typically performs better in terms of sensitivity. The WS can be roughly calculated using the following equation [3].

$$S_\lambda(\lambda) = \frac{\Delta\lambda_{peak}}{\Delta n_a} \tag{5}$$

where Δn_a denotes the analyte RI variation and $\Delta\lambda_{peak}$ the shifting of resonant wavelength. Due to the increment of sample RI, the resonant wavelength red shifts and the index difference of core mode and SPP mode becomes smaller, and hence results in the variation of confinement loss [36]. The sensor shows the highest WS and the sensing resolution of 12500 nm/RIU and 8.0×10^{-6} RIU (by considering the wavelength resolution of 0.1 nm) using the wavelength interrogation method [30]. The resonant peak wavelengths are found at 553, 559, 567, 576, 585, 597, 610, 630, 651, 690, 745 and 870 nm, while the wavelength sensitivities of the proposed sensor are 600, 800, 900, 900, 1200, 1300, 2000, 2100, 3900, 5500, and 12500 nm/RIU for the sample RI from 1.29 to 1.40 respectively. The variation of sample RI could affect the n_{eff} of SPP mode, core mode, and the penetration depth of the SPP field. For practical use, a calibration component is needed for each range of samples' refractive index. Another important sensing parameter for SPR based sensor is AS, which is more likely to be an affordable technique than wavelength interrogation [27]. Since the WS methodology uses the entire wave spectrum, this method and its applications are expensive. On the other hand, due to its ability to determine at a single wavelength, the amplitude interrogation approach is therefore regarded as the most cost-effective technique [32]. The AS can be calculated by the following equation [3].

$$S_\lambda\left(RIU^{-1}\right) = -\frac{1}{\alpha\left(\lambda n_a\right)} \frac{\delta\alpha\left(\lambda n_a\right)}{\delta n_a} \tag{6}$$

where the loss depth is denoted by $\alpha(\lambda n_a)$ and is considered at any sample RI, and the distinction of the two corresponding loss spectra are denoted by $\delta\alpha(\lambda n_a)$. The AS of the suggested

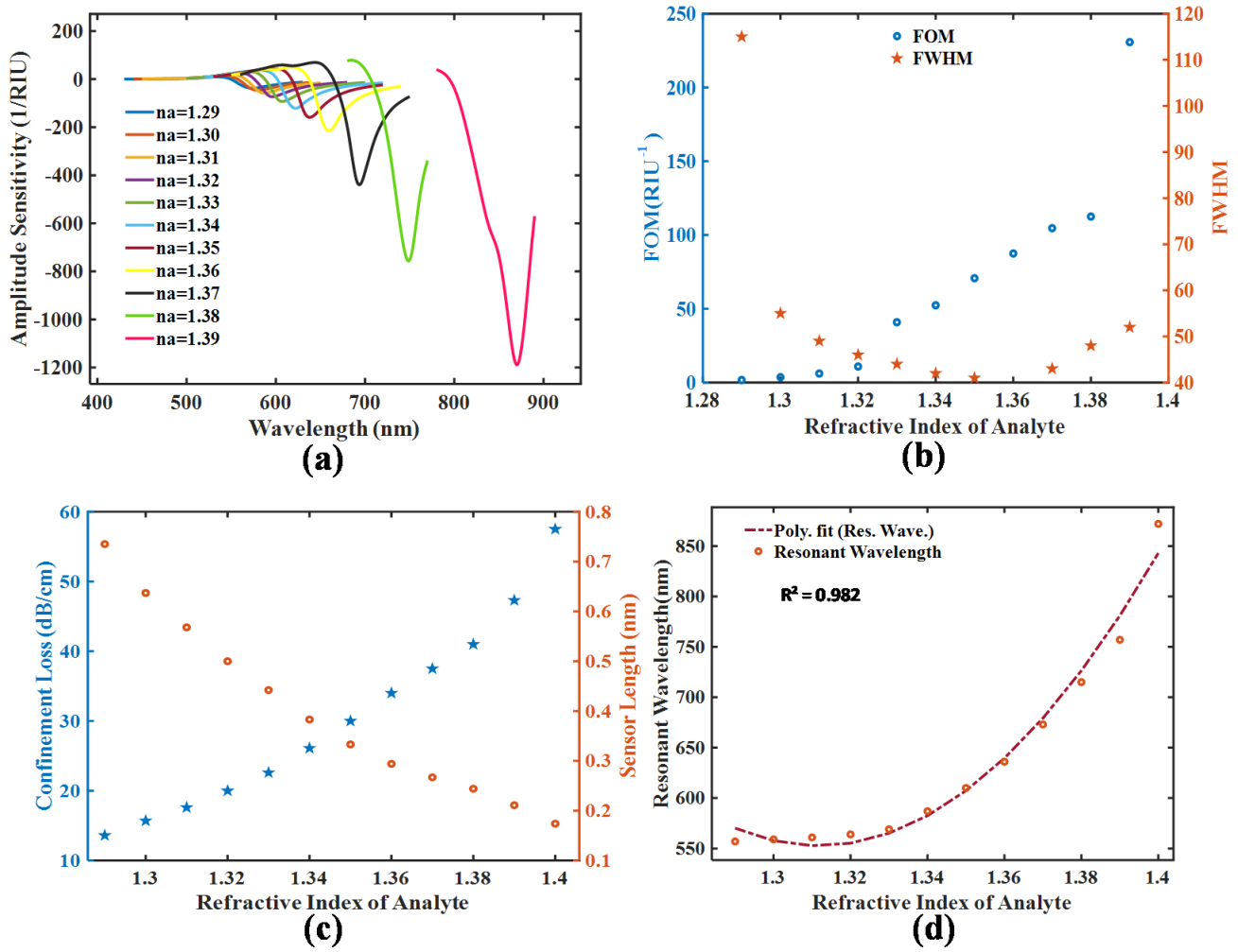

FIGURE 5. The plots of (a) Amplitude sensitivities (b) correlation between FOM and FWHM for the variation of sample RI, (c) Confinement loss and sensor length, and (d) Polynom Fitting for the introduced model.

sensor, which was determined by changing the sample RI, is depicted in Fig. 5(a). Based on the figure, the AS values of the sensor are elevated in line with the increment of the sample RI by a specific difference of 0.01. The analyte with a RI of 1.39 was identified at 881 nm, and the maximum AS of the suggested model is 1189 RIU^{-1}. Another significant parameter of the SPR sensor is the resolution of the sensor, which means the detection capability during the detection of the smallest variation in analyte RI. The accuracy of a SPR sensor may be significantly less desirable as compared to its resolution. The sensor's resolution can be determined by the following equation [37].

$$R(RIU) = \Delta n_a \times \frac{\Delta\lambda_{m!n}}{\Delta\lambda_{\text{peak}}} \tag{7}$$

where the minimum spectrum resolution is pointed out by $\Delta\lambda_{\text{min}}$ while $\Delta\lambda_{\text{peak}}$ denotes the resonant wavelength peak shift. In our proposed sensor, the magnitudes of the several parameters are $\Delta n_a = 0.01$, $\Delta\lambda_{\text{min}} = 0.1$ nm, and $\Delta\lambda_{\text{peak}} = 125$ nm. By assuming the magnitude of minimum transmitted light intensity as 1% to be detected appropriately, we obtained a very high-resolution value of 8.0×10^{-6} RIU for our proposed sensor. Usually, the sensitivity performance of a PCF-SPR sensor rely on the evanescent field, since a very intense evanescent field may cause the severe transmission loss in the fiber [17].

B. FIGURE OF MERIT (FOM) & POLYNOMIAL FITTING

Several significant parameters such as FOM and signal–to–noise ratio (SNR) are also responsible for describing the quality of the sensor. These parameters are related to the full width at half maximum (FWHM) also represented as ($\Delta\lambda_{1/2}$) and can be expressed as [38].

$$FOM = \frac{S_\lambda}{\Delta\lambda_{1/2}} \tag{8}$$

$$SNR = \frac{\Delta\lambda_{\text{peak}}}{\Delta\lambda_{1/2}} \tag{9}$$

The maximum FOM and FWHM values of the proposed sensor are 240.39 RIU^{-1} and 115 nm, respectively. In Fig. 5(b), the values of FOM and FWHM with respect

TABLE 2. The performance of the proposed sensor for y polarized mode.

Analyte RI	Res. Wave. (nm)	Peak Loss (dB/cm)	Res. Shift (nm)	Wave. Sens. (nm/RIU)	Ampl. Sens. (RIU^{-1})	FWHM (nm)	FOM (RIU^{-1})	SNR	Wave. Res. (RIU)	DL (RIU^2/nm)
1.29	553	13.6	6	600	32	115	5.22	0.052	1.67×10^{-4}	1.33×10^{-8}
1.30	559	15.7	8	800	41	55	14.55	0.145	1.25×10^{-4}	1.00×10^{-8}
1.31	567	17.6	9	900	58	49	18.37	0.184	1.11×10^{-4}	8.89×10^{-9}
1.32	576	20	9	900	73	46	19.57	0.196	1.11×10^{-4}	8.89×10^{-9}
1.33	585	22.6	12	1200	92	44	27.27	0.273	8.33×10^{-5}	6.67×10^{-9}
1.34	597	26.1	13	1300	120	42	30.95	0.310	7.69×10^{-5}	6.15×10^{-9}
1.35	610	30	20	2000	159	41	48.78	0.488	5.00×10^{-5}	4.00×10^{-9}
1.36	630	34	21	2100	214	40	52.50	0.525	4.76×10^{-5}	3.81×10^{-9}
1.37	651	37.5	39	3900	440	43	90.70	0.907	2.56×10^{-5}	2.05×10^{-9}
1.38	690	41	55	5500	756	48	114.58	1.146	1.82×10^{-5}	1.45×10^{-9}
1.39	745	47.3	125	12500	1189	52	240.39	2.404	8.00×10^{-6}	6.4×10^{-10}
1.40	870	57.5	N/A	N/A	N/A	59	N/A	N/A	N/A	N/A

to the change in RI of the sample are presented. According to this figure, the values of FWHM steadily decrease as analyte RI increases. Additionally, because the FOM is the ratio of WS to FWHM, it exhibits inverse characteristics. Additionally, the FOM also implies the output proficiency of the sensors. However, the maximum values of FOM and FWHM were observed at analyte RIs of 1.40 and 1.29, respectively, and FOM should be as high as possible for an SPR sensor with high sensitivity. Equation 9 provided us with the maximum and minimum SNR values of 0.052 and 2.404 respectively.

The relationship between the proposed sensor's length and loss depth is depicted in Fig. 5(c), where sensor length is inversely proportional to confinement loss and vice versa. The provided model precisely reveals the detection sensitivity of an unknown liquid's RI, which is restricted to a few centimeters to millimeters. The length of the sensor may be constrained by the extreme confinement loss, if the loss depth is too large, and incident light may provide an undetected signal in the system output. Once we set the incidence light, it can also all of a sudden become invisible. Whatever the case, the sensor's loss depth also reveals the coupling strength. If it is too low, the performance of the sensor will also degrade. Additionally, the proposed sensor offers superior sensitivity performance with regards to the forward fluctuation of the sample RI [21], [39], [40] due to the strong light coupling strength. As a result, we should modify it to optimize the sensor to achieve the lowest possible confinement loss. Because the analyte RI moves forward in the PCF-SPR sensor, the propagation loss and resonant point shifts forward [41]. For the RIs of 1.29 and 1.40, respectively, the sensor length is 0.74 mm and 0.17 mm at its highest and lowest values.

The second order polynomial curve fitting of the model is displayed in Fig. 5(d). We obtained the R2 value of 0.982, which means that this is a highly responsive sensor and achieves high accuracy [42]. Table 2 provides a detailed illustration of the proposed sensor's characteristics, allowing us to understand the significance of this model.

IV. FIBER CORE AND FABRICATION TOLERANCE

A. FIBER CORE OPTIMIZATION

For the stimulation of the sensing channels and the transmission of light, the fiber core plays a vital role. We have additionally optimized the effect of SCD air holes on light propagation for the sample RIs of 1.35 and 1.36, as shown in Fig. 6. First, by eliminating the central air hole in Fig. 6(a), we have optimized for a solid core. Thus, for RIs of 1.35 and 1.36, respectively, the externally existing sensing channel exhibits extremely low confinement losses of 2.4 dB/cm and 0.2 dB/cm at 608 nm and 609 nm respectively. Additionally, compared to the proposed model, the wavelength and AS for the solid core are very low at 100 nm/RIU and 91 RIU^{-1}, respectively. Second, we optimized by leaving the smallest SCD air hole in place and removing the four smaller SCD air holes from the central air hole's upper and lower sides (see Fig. 6(b)).

The model depicts loss depth of 21 dB/cm and 1.3 dB/cm at 606nm and 609 nm for RI of 1.35 and 1.36 respectively with strong coupling intensity. However, the wavelength and AS for omitted SCD air holes investigation has moderate values of 300 nm/RIU and 94 RIU^{-1} respectively. Finally, smallest, and smaller SCD air holes are replaced in the reverse position (see Fig. 6(c)). In case of this optimization, the model shows high confinement loss compared with Fig. 6(a) and Fig. 6(b) which is around 38 dB/cm and 3.2 dB/cm at 610nm and 613 nm for RIs of 1.35 and 1.36 respectively. Since the sensing signal in the output system dissipates instantly after launching the incident light, the significant confinement loss restricts the fiber length and makes it impossible to measure in practice. The wavelength and AS for reversing SCD air holes investigation has almost similar values as compared to omitted investigation, of 300 nm/RIU and 92 RIU^{-1} respectively. However, the SCD air holes are taken into consideration when creating the light-transmitting core. This strongly implies that the air hole distribution performs the best when compared to the other designs as illustrated in Table 3 in order to obtain a high sensitivity response from the suggested design of the core.

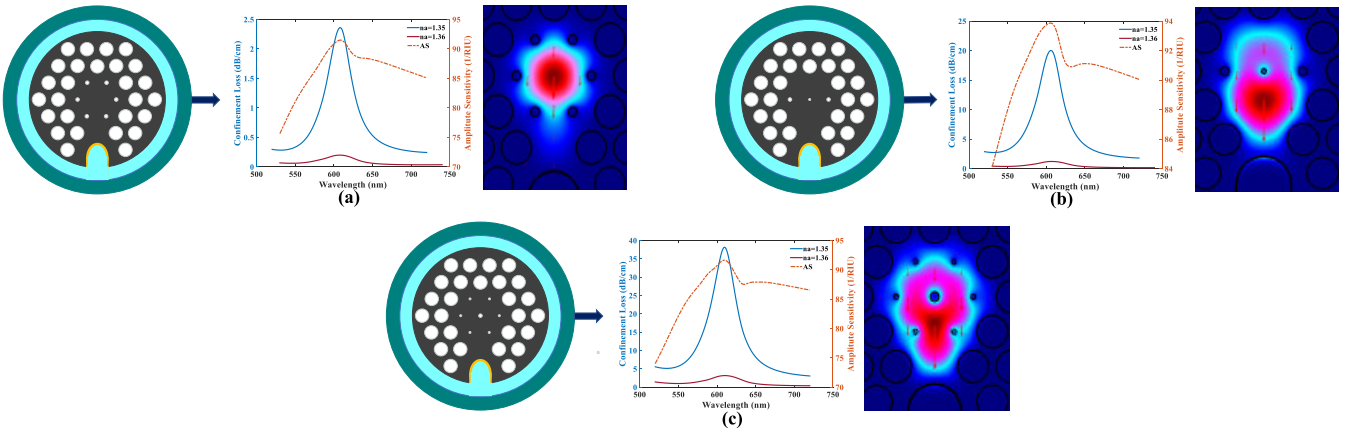

FIGURE 6. The light distribution effect optimization of SCD air holes in several possible ways for the sample RI of 1.35 and 1.36. (a) Omitted center scaled-down air holes. (b) kept center scaled-down air-hole and omitted four air holes from both upper and lower sides, and (c) position reversing of smallest and smaller scaled-down air-holes.

TABLE 3. Fiber core optimization.

Fiber Core Investigation	WS (nm/RIU)	AS (RIU^{-1})
Solid Core	100	91
Omitted Core	300	94
Reversing Core	300	92
Proposed Core	2000	159

B. METAL OPTIMIZATION

The depth of the gold coating affects the detecting abilities. Fig. 7(a) illustrates the red shifting characteristics of the loss spectrum of such a proposed sensor with increase in gold layer thickness and demonstrates that the change in sensing performance is a result of layer thickness. Peak losses of 32 dB/cm and 35 dB/cm were discovered for the sample RI of 1.35 and 1.36, respectively, at 667 nm and 686 nm, which are 6.67% and 3% higher than the values discovered for the proposed thickness of $t_g = 45$ nm. Similarly, for the same RI, the minimum losses of 26 dB/cm and 28 dB/cm were found at $t_g = 40$nm that occurred at 565 nm and 581 nm respectively which are 13.3% and 6.67% less than optimum values. In the case of Au, the phase matching wavelength is redshifted as a result of an increase in layer depth, which raises the effective refractive index (n_{eff}) of the SPP mode. Additionally, as the gold layer gets thicker, the lossdepth likewise gets increasingly deeper. Similar results were seen for the AS, as shown in Fig. 7(b), where the AS gradually grows as a result of the expansion of the gold layer. Additionally, a higher gold metal damping loss may result from the thicker gold layer. The maximum AS is discovered for the gold thickness of $t_g = 50$ nm, and is 166 RIU^{-1} at 696 nm resonant wavelength, which is 4.5% higher than the ideal value of 159 RIU^{-1}. When the gold thickness is 40 nm, the AS steadily declines to 114 RIU^{-1}, which is -28.3% of the optimal value as seen in Fig. 7 (c).

C. PITCH VALUE OPTIMIZATION

Additionally, we have included manufacturing tolerances in the performance study to improve the efficiency of the proposed sensor. Figure 8 (a) depicts the variation in confinement loss as a result of structural modification in pitch size. When the pitch size is altered by 10% from the optimal value of 2.2 m, the sensor shows reduced variation influence on loss depth. Confinement losses at +10% and +5% of optimal pitch are respectively, 16.7%, 10% and 25 dB/cm and 27 dB/cm below optimal values, respectively, at 610 nm and 611 nm. For 5% and 10% decrement of pitch, the losses found are 34 dB/cm and 36 dB/cm at 613 nm and 612 nm respectively, which are successively 13.3% and 20% higher than optimum values.

Besides, the loss spectrum seems to steadily diminish as the pitch size increases, and vice versa. In addition, when the wavelength is reduced, the peak wavelength red shifts and vice versa. Fig. 8(b) demonstrates the small effect in wavelength interrogation due to pitch size variation from −10% to +10%. We obtained the wavelength sensitivities of 2000, 1900, 2000, 1900, and 1900 nm/RIU for successive variations.

D. AIR HOLES DIAMETER OPTIMIZATION

The effect of shifting configurational parameter values, which may or may not be severe in the case of air hole diameter, can be reliably predicted from pitch value optimization. The spectrum depth for a thick air hole diameter variation of 10% is shown in Fig. 8(c), where the loss depths are nearly equal to the optimal depth. We obtained loss depths of 28.4 and 29.4 dB/cm at 611 and 609 nm, respectively, which are 5% and 2% lower than their corresponding optimum values, by adding 5% and 10% to the recommended magnitude (d = 1.76 m). Additionally, we discovered loss depths of 31 and 32 dB/cm at 611 and 612 nm, respectively, for 5% and 10% decrement, which are 5% and 2% greater than their corresponding optimum values. The loss depths increase slightly

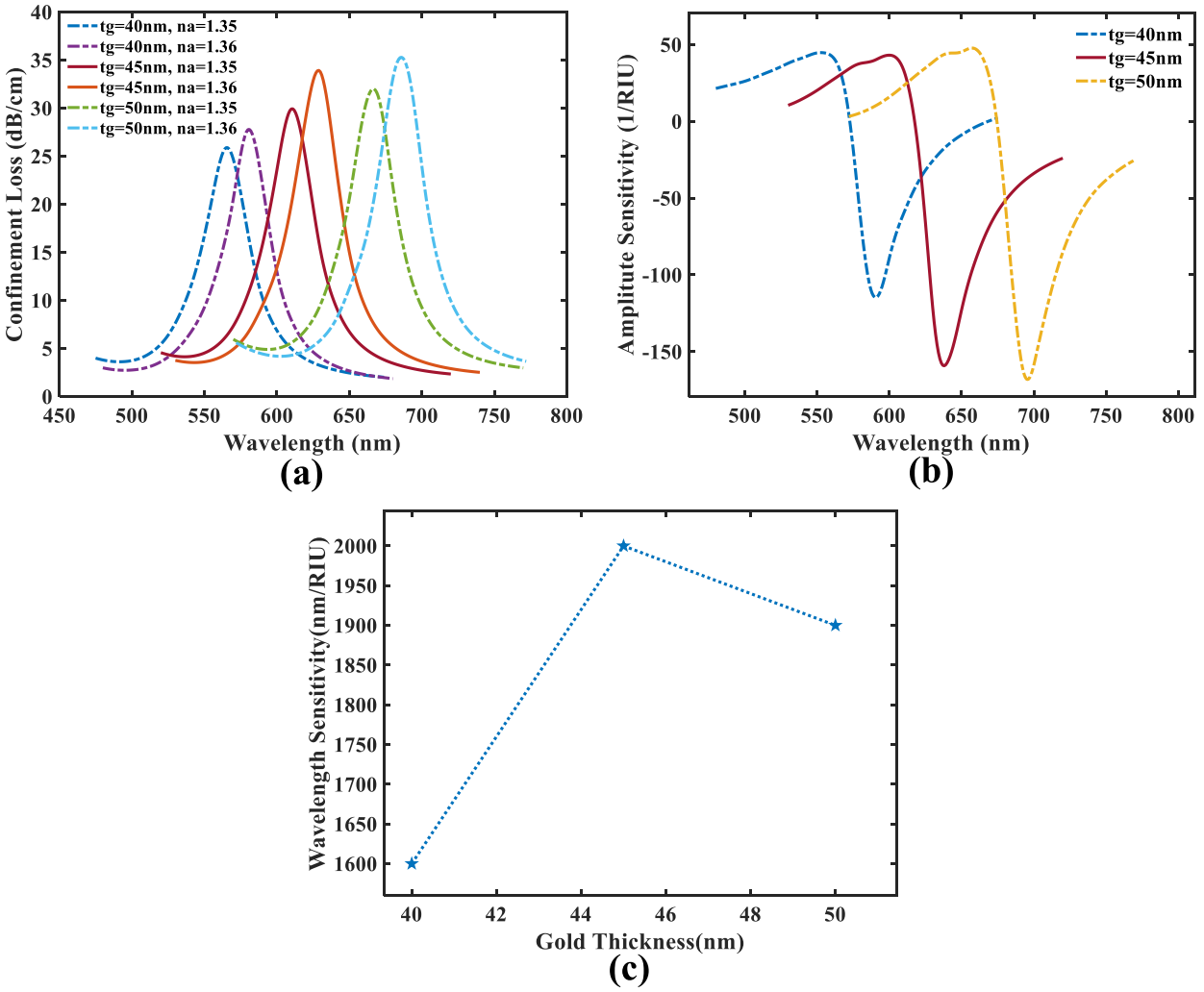

FIGURE 7. For the miscellaneous depth of gold layer (a) Loss spectrum (b) AS curves and (c) Resonant wavelength interrogation curve for gold layer's thickness variation.

as the size of the SCD air-hole decreases. This increased light confinement spreads with the aid of an asymmetric-core guided formation. As a result, more light can interact with the metal layer, stimulating SPP modes. As a result, no significant resonance wavelength shifting happens as the width of the air hole changes. Figure 8(d) illustrates how the d value fluctuation from −10% to +10% has less of an impact on wavelength interrogation. For sequential variation, we obtained the wavelength sensitivities of respectively 1900, 1900, 2000, 1800, and 1900 nm/RIU.

Fig. 9(a) shows the sensor's performance or loss spectrum impact as a function of thin SCD air hole dimensions modification (tiny SCD air holes that are taken into consideration along the asymmetric-core formation). Even when the optimal diameter ($d_s = 0.5\ \mu m$) is increased or lowered by ±10%, the spectrum depth is nearly identical to the optimum value. As the size of the SCD air-hole is reduced, the depth of the loss grows progressively. For +10, +5, −5, and −10% variations, the loss depths are 32, 31, 29, and 28 dB/cm at 612, 611, 61, and 610 nm respectively. The successive loss depths are +6.67%, +3.3%, −3.3% and −6.67% higher or lower than optimal value (30 dB/cm). As a result, there are no major changes in loss depths, and resonance frequency shifting takes place as the width of the air holes change. Fig. 9(b) depicts the effect on wavelength interrogation due to the d_s value variations that causes the dc value variation from −10 to +10%.

Fig. 9(c) shows the performance of the sensor or the loss spectrum impact as a function of the narrower SCD air hole diameter. There are very small spectrum intervals among optimized curves even though the proposed diameter (dc = 0.264 μm) is increased or decreased by ±10%. Loss depth rises gradually according to the increment of SCD air-hole size. For +10, +5, −5, and −10% variations, the loss depths are 32, 31.3, 29.2, and 28.4 dB/cm at 612, 611, 611, and 610 nm respectively. The successive loss depths are +6.6, +4.3, −2.6 and −5.3% higher or lower than optimal value (30 dB/cm). Overall, there is almost no significant loss depth

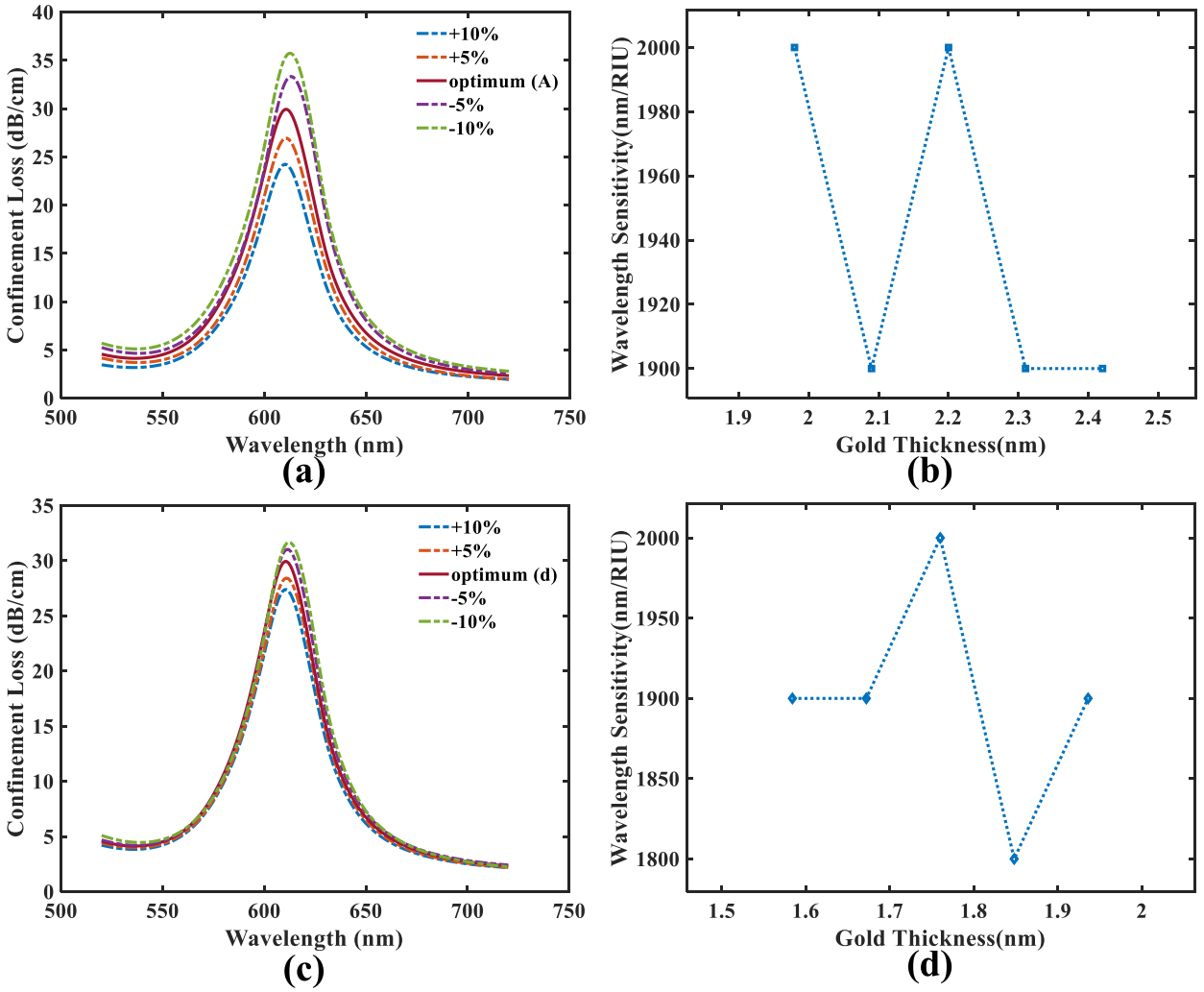

FIGURE 8. (a) Fluctuation of loss spectrum curves (b) Resonant wavelength interrogation curve for optimization of pitch size variations (c) Fluctuation of loss spectrum curves and, (b) Resonant wavelength interrogation curve for optimization of thick air holes diameter variations.

TABLE 4. Performance comparison of the proposed sensor with formarly reported sensors.

Ref.	Structure Type	No. of Simulta. Detections	Detection Range (RIU)	Max. Loss (dB/cm)	Operating Wavelength (nm)	WS (nm/RIU)	AS (RIU^{-1})	FOM (RIU^{-1})	Wave. Res. (RIU)
[27]	Dual Polarized Propagation Controlled Sensor	1	1.33-1.39	128	560-1250	15,400	852, 654	N/A	6.49 X 10^{-6}
[43]	Segmented Ag - TiO_2 PCF SPR sensor	1	1.33-1.36	-	500-850	10,600	633.4	303	9.43 X 10^{-6}
[44]	Nanowire-based pentagonal sensor	1	1.32–1.38	180	700–1200	10,286	544	149,6	9.72 X 10^{-6}
[18]	Dual-coated D-shaped sensor	1	1.30–1.38	455	2300–3500	10,000	15	N/A	2.00 X 10^{-5}
[19]	Au-Ag layered multi analyte RI sensor	2	1.33-1.366	530	400-800	2500 (Ch-1) 3083 (Ch-2)	N/A	N/A	3.20 X 10^{-5}
[45]	Graphene-based PCF sensor	1	1.33-1.35	231	N/A	2520	72.5	N/A	3.97 X 10^{-5}
[46]	Hybrid PCF based SPR sensor	2	1.33-1.40 1.33-1.39	-	500-1100 460-1050	12,000 (Ch-1) 10,000 (Ch-2)	807 569	N/A	8.33 X 10^{-6} 1.00 X 10^{-5}
[47]	Optical fiber based SPR sensor	1	1.3666-1.3683	-	N/A	1963	334	N/A	5.09 X 10^{-5}
This work	Novel structured annular shaped sensor	1	1.29-1.40	57.5	420-950	12,500	1189	273.4	8.00 X 10^{-6}

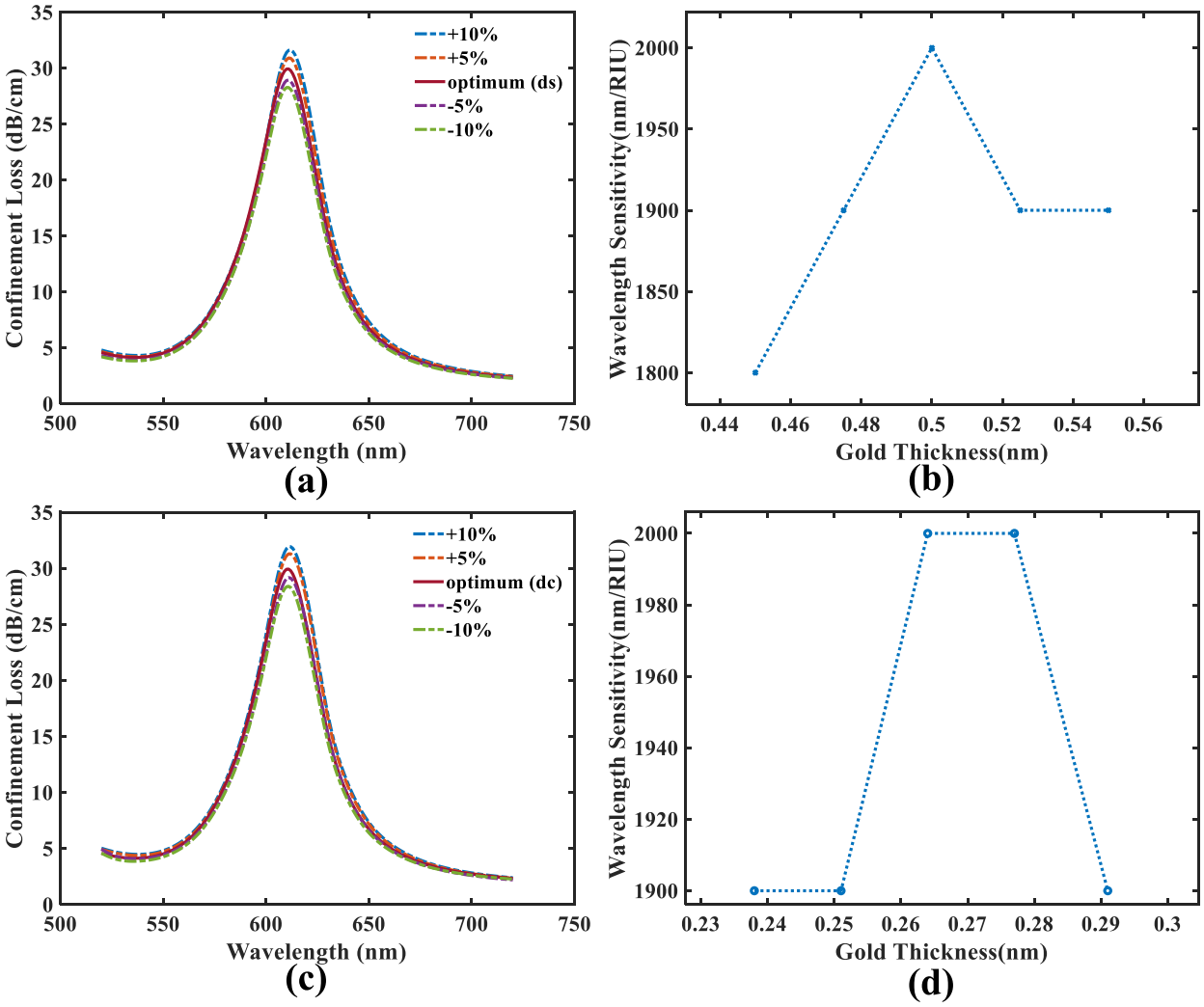

FIGURE 9. (a) Fluctuation of loss spectrum curves (b) Resonant wavelength interrogation curve for optimization of thin air holes diameter variations (c) Fluctuation of loss spectrum curves (b) Resonant wavelength interrogation curve for optimization of thinner air holes diameter variations.

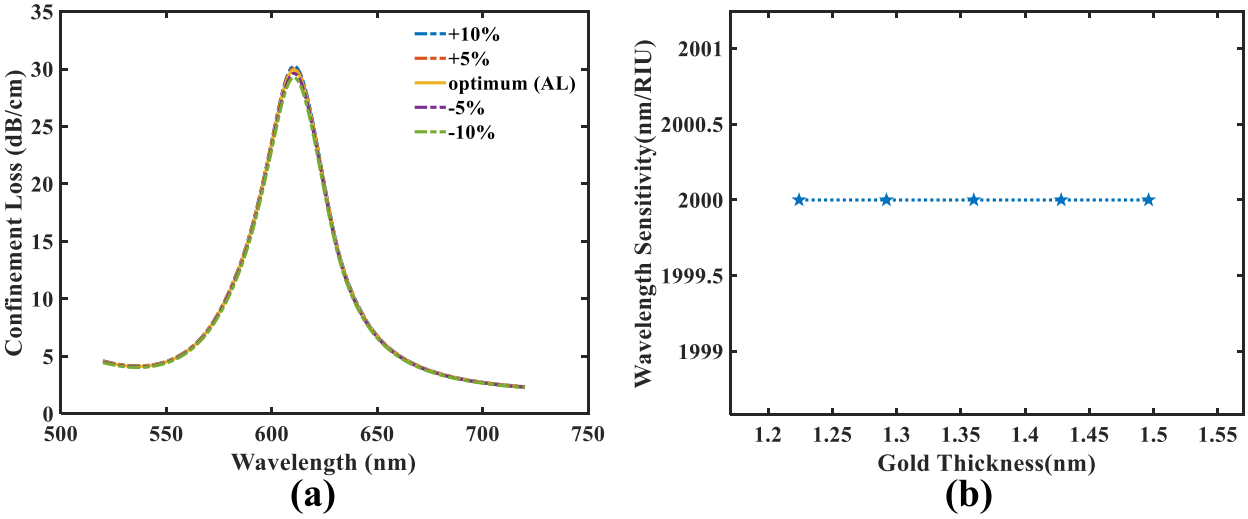

FIGURE 10. (a) Fluctuation of loss spectrum curves and, (b) Resonant wavelength interrogation curve for optimization of hin air holes diameter variations.

variations and resonant wavelength shifting due to the diameter variations in the air holes. Fig. 9(d) depicts the wavelength variation due to the dc value variation from −10 to +10%.

E. ANALYTE LAYER OPTIMIZATION

Fig. 10 (a) illustrates that there are nearly no spectrum depth differences for the optimum value of analyte layer variations by ±5% to ±10% ($t_{AL} = 1.36\ \mu m$). In this case, peak magnitudes of loss curves increase gradually with the enhancement of sample layer depth. As a consequence, more light comes in contact with the metallic surface, causing the SPP modes to be energized. For ±10% variations, resonant wavelengths for those corresponding variations almost remain comparable when compared to the optimum resonant case. Here 611 nm is the optimum resonant wavelength for the proposed thickness. In contrast, with the decrement of −10% and −5%, the peak loss magnitudes are at 29.26 and 29.63 dB/cm respectively which are only 5% and 4% less than optimum value and both the resonant peaks appears at 610 nm. Similarly, for the +10% and +5% changes, the peak loss values are 30.26 and 30.07 dB/cm, which is only 2.2% and 2.7% higher than optimum value and both the resonant peaks appears at 610 nm. Therefore, no significant propagation loss and resonance wavelength shifting occur with diameter variations of the air holes. Fig. 10 (b) depicts the effect in wavelength variation due to the Au thickness variations. A WS of 2000 nm/RIU is obtained for all corresponding variations that are similar to the optimal value.

V. CONCLUSION

In this study, a special symmetric and hexagonal core PCF-SPR sensor is demonstrated in order to determine how plasmonic sensing is controlled by propagation. To attain maximum sensitivity, the optimal measurable forming factors of the proposed model are numerically examined using FEM. The sensor exhibits an extreme sensitivity of 1189 RIU^{-1} for the amplitude interrogation technique, while having a remarkable sensitivity and resolution of 12,500 nm/RIU and 8.0×10^{-6} RIU respectively. Furthermore, the claimed sensor is still capable of detecting unknown analyte RI even when the sample RI has a smallest scale change of around 10^{-6} in the sensing range of 1.29 to 1.40. To execute the detection performance and account for the changing structural qualities during manufacturing, the model parameters are altered up to 10% from their intended value. We predict that the suggested asymmetric-core guided PCF-SPR sensor will be a good model for POC applications in detecting glucose, viruses, DNA/RNA, and proteins among other things, since it has proven exceptional sensing qualities with a simple design.

REFERENCES

[1] B. Han, Y.-N. Zhang, X. Wang, D. Yang, Y. Liu, J. Sun, and Y. Wang, "High-sensitive fiber anemometer based on surface plasmon resonance effect in photonic crystal fiber," *IEEE Sensors J.*, vol. 19, no. 9, pp. 3391–3398, May 2019, doi: 10.1109/JSEN.2019.2895265.

[2] D. Liu. *Highly Sensitive Twist Sensor Based on Partially Silver Coated Hollow Core Fiber Structure*. Accessed: Jun. 27, 2022. [Online]. Available: https://opg.optica.org/jlt/abstract.cfm?uri=jlt-36-17-3672

[3] E. K. Akowuah, T. Gorman, H. Ademgil, S. Haxha, G. K. Robinson, and J. V. Oliver, "Numerical analysis of a photonic crystal fiber for biosensing applications," *IEEE J. Quantum Electron.*, vol. 48, no. 11, pp. 1403–1410, Nov. 2012, doi: 10.1109/JQE.2012.2213803.

[4] F. Haider, R. A. Aoni, R. Ahmed, W. J. Chew, and G. A. Mahdiraji, "Alphabetic-core assisted microstructure fiber based plasmonic biosensor," *Plasmonics*, vol. 15, no. 6, pp. 1949–1958, Jul. 2020, doi: 10.1007/S11468-020-01220-9.

[5] F. Poli, A. Cucinotta, and S. Selleri, *Photonic Crystal Fibers: Properties and Applications*, vol. 102. Berlin, Germany: Springer, 2007.

[6] D. A. Krohn, T. MacDougall, and A. Mendez, *Fiber Optic Sensors: Fundamentals and Applications*. Bellingham, WA, USA: SPIE, 2014.

[7] A. A. Rifat, R. Ahmed, A. K. Yetisen, H. Butt, A. Sabouri, G. A. Mahdiraji, S. H. Yun, and F. R. M. Adikan, "Photonic crystal fiber based plasmonic sensors," *Sens. Actuators B, Chem.*, vol. 243, pp. 311–325, May 2017, doi: 10.1016/J.SNB.2016.11.113.

[8] L. H. Rindorf, J. B. Jensen, and M. Dufva, "Photonic crystal fiber long-period gratings for biochemical sensing," *Opt. Exp.*, vol. 14, no. 18, pp. 8224–8231, Jul. 2006, doi: 10.1364/OE.14.008224.

[9] S. W. James and R. P. Tatam, "Optical fibre long-period grating sensors: Characteristics and application," *Meas. Sci. Technol.*, vol. 14, no. 5, pp. 49–61, Mar. 2003, doi: 10.1088/0957-0233/14/5/201.

[10] A. A. Rifat, F. Haider, R. Ahmed, G. A. Mahdiraji, F. R. M. Adikan, and A. E. Miroshnichenko, "Highly sensitive selectively coated photonic crystal fiber-based plasmonic sensor," *Opt. Lett.*, vol. 43, no. 4, pp. 891–894, 2018, doi: 10.1364/OL.43.000891.

[11] B. Liedberg, C. Nylander, and I. Lunström, "Surface plasmon resonance for gas detection and biosensing," *Sens. Actuators*, vol. 4, pp. 299–304, Jan. 1983, doi: 10.1016/0250-6874(83)85036-7.

[12] B. Liedberg, C. Nylander, and I. Lundström, "Biosensing with surface plasmon resonance—How it all started," *Biosens. Bioelectron.*, vol. 10, no. 8, pp. 1–9, Jan. 1995, doi: 10.1016/0956-5663(95)96965-2.

[13] J. Homola, I. Koudela, and S. S. Yee, "Surface plasmon resonance sensors based on diffraction gratings and prism couplers: Sensitivity comparison," *Sens. Actuators B, Chem.*, vol. 54, nos. 1–2, pp. 16–24, Jan. 1999, doi: 10.1016/S0925-4005(98)00322-0.

[14] J. Homola and M. Piliarik, *Surface Plasmon Resonance (SPR) Sensors*. Springer, 2006, pp. 45–67, doi: 10.1007/5346_014.

[15] J. N. Dash and R. Jha, "Graphene-based birefringent photonic crystal fiber sensor using surface plasmon resonance," *IEEE Photon. Technol. Lett.*, vol. 26, no. 11, pp. 1092–1095, Jun. 2014, doi: 10.1109/LPT.2014.2315233.

[16] N. Ayyanar, K. V. Sreekanth, G. T. Raja, and M. S. M. Rajan, "Photonic crystal fiber-based reconfigurable biosensor using phase change material," *IEEE Trans. Nanobiosci.*, vol. 20, no. 3, pp. 338–344, Jul. 2021.

[17] N. Jahan, M. M. Rahman, M. Ahsan, M. A. Based, M. M. Rana, S. Gurusamy, and J. Haider, "Photonic crystal fiber based biosensor for pseudomonas bacteria detection: A simulation study," *IEEE Access*, vol. 9, pp. 42206–42215, 2021, doi: 10.1109/ACCESS.2021.3063691.

[18] V. Kaur and S. Singh, "Design of D-shaped PCF-SPR sensor with dual coating of ITO and ZnO conducting metal oxide," *Optik*, vol. 220, Oct. 2020, Art. no. 165135, doi: 10.1016/J.IJLEO.2020.165135.

[19] M. A. Jabin, K. Ahmed, M. J. Rana, B. K. Paul, M. Islam, D. Vigneswaran, and M. S. Uddin, "Surface plasmon resonance based titanium coated biosensor for cancer cell detection," *IEEE Photon. J.*, vol. 11, no. 4, pp. 1–10, Aug. 2019, doi: 10.1109/JPHOT.2019.2924825.

[20] M. B. Hossain, M. S. Hossain, S. M. R. Islam, M. N. Sakib, K. Z. Islam, M. A. Hossain, M. Sanwar Hossain, A. S. M. S. Hosen, and G. H. Cho, "Numerical development of high performance quasi D-shape PCF-SPR biosensor: An external sensing approach employing gold," *Results Phys.*, vol. 18, Sep. 2020, Art. no. 103281, doi: 10.1016/j.rinp.2020.103281.

[21] V. Kaur and S. Singh, "Design of titanium nitride coated PCF-SPR sensor for liquid sensing applications," *Opt. Fiber Technol.*, vol. 48, pp. 159–164, Mar. 2019, doi: 10.1016/j.yofte.2018.12.015.

[22] M. H. K. Anik, M. I. A. Isti, S. M. R. Islam, S. Mahmud, H. Talukder, M. J. Piran, S. K. Biswas, and K.-S. Kwak, "Milled microchannel-assisted open D-channel photonic crystal fiber plasmonic biosensor," *IEEE Access*, vol. 9, pp. 2924–2933, 2021, doi: 10.1109/ACCESS.2020.3047509.

[23] J. N. Dash and R. Jha, "SPR biosensor based on polymer PCF coated with conducting metal oxide," *IEEE Photon. Technol. Lett.*, vol. 26, no. 6, pp. 595–598, Mar. 2014, doi: 10.1109/LPT.2014.2301153.
[24] M. Rachana, I. Charles, S. Swarnakar, S. V. Krishna, and S. Kumar, "Recent advances in photonic crystal fiber-based sensors for biomedical applications," *Opt. Fiber Technol.*, vol. 74, Dec. 2022, Art. no. 103085.
[25] C. Caucheteur, T. Guo, and J. Albert, "Review of plasmonic fiber optic biochemical sensors: Improving the limit of detection," *Anal. Bioanal. Chem.*, vol. 407, no. 14, pp. 3883–3897, May 2015, doi: 10.1007/s00216-014-8411-6.
[26] C. Liu, W. Su, X. Lu, F. Wang, T. Sun, and P. K. Chu, "Symmetrical dual D-shape photonic crystal fibers for surface plasmon resonance sensing," *Opt. Exp.*, vol. 26, no. 7, pp. 9039–9049, 2018, doi: 10.1364/OE.26.009039.
[27] A. M. T. Hoque, A. Islam, F. Haider, H. A. B. A. Rashid, R. Ahmed, and R. A. Aoni, "Dual polarized surface plasmon resonance refractive index sensor via decentering propagation-controlled core sensor," *Opt. Continuum*, vol. 1, no. 7, p. 1474, Jun. 2022, doi: 10.1364/OPTCON.460520.
[28] F. Haider, R. A. Aoni, R. Ahmed, M. S. Islam, and A. E. Miroshnichenko, "Propagation controlled photonic crystal fiber-based plasmonic sensor via scaled-down approach," *IEEE Sensors J.*, vol. 19, no. 3, pp. 962–969, Feb. 2019, doi: 10.1109/JSEN.2018.2880161.
[29] M. F. O. Hameed, Y. K. A. Alrayk, A. A. Shaalan, W. S. El Deeb, and S. S. A. Obayya, "Design of highly sensitive multichannel bimetallic photonic crystal fiber biosensor," *J. Nanophotonics*, vol. 10, no. 4, Dec. 2016, Art. no. 046016, doi: 10.1117/1.JNP.10.046016.
[30] M. R. Hasan, S. Akter, A. A. Rifat, S. Rana, K. Ahmed, R. Ahmed, H. Subbaraman, and D. Abbott, "Spiral photonic crystal fiber-based dual-polarized surface plasmon resonance biosensor," *IEEE Sensors J.*, vol. 18, no. 1, pp. 133–140, Jan. 2018, doi: 10.1109/JSEN.2017.2769720.
[31] A. A. Rifat, G. Mahdiraji, Y. M. Sua, R. Ahmed, Y. Shee, and F. M. Adikan, "Highly sensitive multi-core flat fiber surface plasmon resonance refractive index sensor," *Opt. Exp.*, vol. 24, no. 3, pp. 2485–2495, 2016, doi: 10.1364/OE.24.002485.
[32] F. Haider, M. Mashrafi, R. Haider, R. A. Aoni, R. Ahmed, and R. Ahmed, "Asymmetric core-guided polarization-dependent plasmonic biosensor," *Appl. Opt.*, vol. 59, no. 26, pp. 7829–7835, Sep. 2020, doi: 10.1364/AO.400301.
[33] *Design and Characterization of Highly Birefringent Residual Dispersion Compensating Photonic Crystal Fiber*. Accessed: Jun. 14, 2022. [Online]. Available: https://opg.optica.org/jlt/abstract.cfm?uri=jlt-32-23-3976
[34] D. Gao, C. Guan, Y. Wen, X. Zhong, and L. Yuan, "Multi-hole fiber based surface plasmon resonance sensor operated at near-infrared wavelengths," *Opt. Commun.*, vol. 313, pp. 94–98, Feb. 2014, doi: 10.1016/J.OPTCOM.2013.10.015.
[35] R. Otupiri, E. K. Akowuah, S. Haxha, H. Ademgil, F. AbdelMalek, and A. Aggoun, "A novel birefrigent photonic crystal fiber surface plasmon resonance biosensor," *IEEE Photon. J.*, vol. 6, no. 4, pp. 1–11, Aug. 2014, doi: 10.1109/JPHOT.2014.2335716.
[36] G. Wang, S. Li, G. An, X. Wang, Y. Zhao, W. Zhang, and H. Chen, "Highly sensitive D-shaped photonic crystal fiber biological sensors based on surface plasmon resonance," *Opt. Quantum Electron.*, vol. 48, no. 1, pp. 1–9, Dec. 2015, doi: 10.1007/S11082-015-0346-4.
[37] A. A. Rifat, G. A. Mahdiraji, Y. M. Sua, Y. G. Shee, R. Ahmed, D. M. Chow, and F. R. M. Adikan, "Surface plasmon resonance photonic crystal fiber biosensor: A practical sensing approach," *IEEE Photon. Technol. Lett.*, vol. 27, no. 15, pp. 1628–1631, Aug. 1, 2015, doi: 10.1109/LPT.2015.2432812.
[38] M. S. A. Gandhi, K. Senthilnathan, P. R. Babu, and Q. Li, "Visible to near infrared highly sensitive microbiosensor based on surface plasmon polariton with external sensing approach," *Results Phys.*, vol. 15, Dec. 2019, Art. no. 102590, doi: 10.1016/J.RINP.2019.102590.
[39] J. Wang, L. Pei, L. Wu, J. Wang, Z. Ruan, and J. Zheng, "A polarization-independent SPR sensor based on photonic crystal fiber for low RI detection," *Plasmonics*, vol. 15, no. 2, pp. 327–333, Oct. 2019, doi: 10.1007/S11468-019-01054-0.
[40] C. Liu, J. Wang, F. Wang, W. Su, L. Yang, J. Lv, G. Fu, X. Li, Q. Liu, T. Sun, and P. K. Chu, "Surface plasmon resonance (SPR) infrared sensor based on D-shape photonic crystal fibers with ITO coatings," *Opt. Commun.*, vol. 464, Jun. 2020, Art. no. 125496, doi: 10.1016/J.OPTCOM.2020.125496.
[41] C. Li, B. Song, Y. Guo, J. Wu, W. Huang, X. Wu, C. Jin, and S. Chen, "Two modes excited SPR sensor employing gold-coated photonic crystal fiber based on three-layers air-holes," *IEEE Sensors J.*, vol. 20, no. 11, pp. 5893–5899, Jun. 2020, doi: 10.1109/JSEN.2020.2972031.
[42] A. Islam, F. Haider, R. A. Aoni, and R. Ahmed, "Plasmonic photonic biosensor: In situ detection and quantification of SARS-CoV-2 particles," *Opt. Exp.*, vol. 30, no. 22, p. 40277, 2022, doi: 10.1364/oe.469937.
[43] H. Fang, C. Wei, D. Wang, L. Yuan, S. Jiao, Z. Bao, and H. Yang, "Research on photonic crystal fiber based on a surface plasmon resonance sensor with segmented silver-titanium dioxide film," *J. Opt. Soc. Amer. B, Opt. Phys.*, vol. 37, no. 3, pp. 736–744, 2020, doi: 10.1364/JOSAB.373395.
[44] Y. Guo, J. Li, S. Li, Y. Liu, S. Zhang, J. Wang, S. Wang, W. Zhang, T. Cheng, and R. Hao, "Dual-polarized optical sensing of microstructure fiber with pentagonal-lattice based on surface plasmon resonance in the near-IR spectrum," *Optik*, vol. 202, Feb. 2020, Art. no. 163671, doi: 10.1016/J.IJLEO.2019.163671.
[45] X. Yang, Y. Lu, B. Liu, and J. Yao, "Analysis of graphene-based photonic crystal fiber sensor using birefringence and surface plasmon resonance," *Plasmonics*, vol. 12, no. 2, pp. 489–496, Jun. 2016, doi: 10.1007/S11468-016-0289-Z.
[46] F. Haider, M. Mashrafi, R. A. Aoni, R. Haider, M. Hossen, T. Ahmed, G. A. Mahdiraji, and R. Ahmed, "Multi-analyte detection based on integrated internal and external sensing approach," *IEEE Trans. Nanobiosci.*, vol. 21, no. 1, pp. 29–36, Jan. 2022, doi: 10.1109/TNB.2021.3108834.
[47] Y. Chen, Q. Xie, X. Li, H. Zhou, X. Hong, and Y. Geng, "Experimental realization of D-shaped photonic crystal fiber SPR sensor," *J. Phys. D, Appl. Phys.*, vol. 50, no. 2, Nov. 2016, Art. no. 025101, doi: 10.1088/1361-6463/50/2/025101.

ABDULLAH MOHAMMAD TANVIRUL HOQUE is currently pursuing the degree with the Department of Electrical and Electronic Engineering, Bangabandhu Sheikh Mujibur Rahman Science and Technology University (BSMRSTU). He is also the Secretary of the IEEE BSMRSTU Student Branch, BSMRSTU, and the President of Ohms Research Club. His current research interests include optical fiber sensors and power electronics.

KUSAY FAISAL AL-TABATABAIE received the B.Sc. degree in electrical and electronics engineering, in 2000, and the M.Sc. and Ph.D. degrees in electronic and telecommunication engineering from Universiti Teknologi Malaysia (UTM), in 2007 and 2013, respectively. Currently, he is an Assistant Professor with the Faculty of Computer Science, Cihan University, Sulaimanya Campus, Iraq. His current research interests include wireless communications, radar, satellites, LMDS, HAPS, broadband wireless access, wireless networking fields, mobile communications, the IoT, and fiber optics.

MD. EAKUB ALI received the B.Sc. and M.Sc. degrees from the Khulna University of Engineering and Technology, Bangladesh. Currently, he is a Lecturer with the Department of Electrical and Electronic Engineering, Bangabandhu Sheikh Mujibur Rahman Science and Technology University, Bangladesh. His current research interest includes optical fiber sensors.

ASAD MUHAMMAD BUTT received the B.S. degree in aerospace engineering from the Institute of Space Technology (IST), Pakistan, in 2006, the M.S. degree in mechanical engineering from the National University of Sciences and Technology (NUST), Pakistan, in 2009, and the Ph.D. degree in mechanical engineering from the King Fahd University of Petroleum and Minerals (KFUPM), Saudi Arabia, in 2017. He joined the Space and Upper Atmosphere Research Commission, Pakistan, from 2006 to 2007. Later, he was appointed as a Lecturer with NUST, from 2009 to 2012, and KFUPM, from 2012 to 2017. He has been a Research Specialist with KFUPM, since 2018. His current research interests include aerospace structures, fiber optic sensing, and bioengineering.

SHEIKH SHARIF IQBAL MITU (Senior Member, IEEE) received the Ph.D. degree in electrical engineering from The University of Manchester (UMIST), Manchester, U.K. He is currently an Associate Professor with the Electrical Engineering Department, King Fahd University of Petroleum and Minerals (KFUPM), Dhahran, Saudi Arabia. His research work was funded by academia, government agencies (KACST and SABIC), and local industry (Schlumberger and Saudi Aramco). His current research interest includes micromillimeter-wave integrated/control circuits. He has more than 100 scholarly publications in refereed journals, conference proceedings, and patents in his research area.

KHURRAM KARIM QURESHI (Senior Member, IEEE) received the B.Sc. degree (Hons.) in electrical engineering from the University of Engineering and Technology, Taxila, Pakistan, in 1999, and the Ph.D. degree in electrical engineering from The Hong Kong Polytechnic University, in 2006. He is currently a Professor with the Electrical Engineering Department and a member of the IRC for Communications Systems and Sensing, King Fahd University of Petroleum and Minerals (KFUPM). His current research interests include optical communications, tunable semiconductor and fiber-based lasers, and fiber sensors.